Figure S1. Extended analysis of tail and limb movement during *Xenopus* frog metamorphosis, related to Figure 1.

A-D. Workflow of SLEAP-based behavioral tracking including imaging setup (**A**), video processing pipeline (**B**), and centroid (**C**) and centered (**D**) SLEAP models for quantification of animal or tail/limb movement, respectively.

E-G. Low and high frequency tail movement across metamorphosis. The dominant low frequency of the tail tip is largely constant with an increase from NF52-55 to NF63-64 (**E**; NF52-55 versus NF63-64, p = 0.001). The amount of tail tip movement in the high frequency bin, represented by the sum power, peaks at NF57-58 and then decreases until NF63-64 (**F**; for NF44-48 versus NF52-55 and NF44-48 versus NF57-58, p = <0.0001; NF52-55 versus NF57-58, p = 0.049; NF57-58 versus NF59-62, p = 0.013; NF57-58 versus NF63-64, p = 0.002). Loss of dominant high frequency at the tail tip from NF44-48 to NF57-58 with no animals displaying a high dominant frequency, and thus no data point, at NF63-64 (**G**; for NF44-48 versus NF52-55 and NF44-48 versus NF57-58, p = <0.0001; NF52-55 versus NF57-58, p = 0.002).

H-J. Extended analysis of the gain of hindlimb movement across frog metamorphosis. From NF57-58 to NF63-64, the knee displays an increased mean angle when moving (**H**; for NF57-58 versus NF59-62, NF57-58 versus NF63-64 and NF59-62 versus NF63-64, p = <0.0001). The amount of movement of the knee in the low frequency bin, represented by the sum power, increases from NF57-58 to NF63-64 (**I**; for NF57-58 versus NF59-62, NF57-58 versus NF63-64 and NF59-62 versus NF63-64, p = <0.0001). The dominant frequency of knee movement also increases from NF57-58 to NF59-62 to juvenile stage, reaching an average of 2.2 Hz (**J**; for NF57-58 versus NF59-62 and NF57-58 versus NF63-64, p = <0.0001; NF59-62 versus juvenile, p = 0.017).

K-P. Gain of forelimb movement across frog metamorphosis. PCA plots represent the position of the forelimb and its range of movement during 256 random frames and show an increase in the range of movement from NF59-62 to juvenile stage (**K**; shoulder, yellow; elbow, orange; wrist, red). Scale bar in **K** indicates the color-code of the first principal component of variation of the aligned forelimb positions. Quantification of the mean angle of the elbow shows an increase across metamorphosis (**L**; for NF59-62 versus NF63-64, NF59-62 versus juvenile, and NF63-64 versus juvenile, p = <0.0001). The range of elbow movement decreases from NF59-62 to juvenile (**M**; NF59-62 versus juvenile, p = 0.046; NF63-64 versus juvenile, p = 0.002). Mean power spectrum of the elbow oscillations for each stage of metamorphosis shows a single peak in the low frequency range (**N**; 0.9-4.5 Hz, dark gray). The amount of movement of the elbow in the low frequency bin, represented by the sum power, increases from NF57-58 to juvenile stage (**O**; for NF59-62 versus NF63-64 andNF59-62 versus juvenile, p = <0.0001). The dominant frequency of elbow movement also increases from NF57-58 to juvenile stage, reaching an average of 2 Hz (**P**; NF59-62 versus NF63-64, p = 0.031; NF59-62 versus juvenile, p = <0.0001).

n = 172 animals for NF37-38; n = 47 animals for NF44-48; n = 24 animals for NF52-55, n = 11 animals for NF57-58, n = 13 animals for NF59-62, n = 8 animals for NF63-64, n = 13 animals for juvenile stage.

Figure S2. Rostrocaudal tail and proximodistal limb movement analysis across metamorphosis, related to Figure 1.

A-I. Range and frequency of movement along the rostrocaudal axis of the tail. SLEAP skeleton (yellow) superimposed onto an image of a recorded animal at NF44-48, NF52-55 and

NF63-64 with all tracked points indicated (**A**; tail top, dark blue; tail mid, blue; tail tip, light blue). The range of movement is initially uniform for all three tail points at NF44-48; however, from NF52-55 to NF63-64, they diverge, with, for example, the tail tip having a greater range than the top (**B**. NF52-55: for top versus tip and mid versus tip, p = <0.0001. NF57-58: for top versus tip and mid versus tip, p = <0.0001. NF59-62: top versus tip, p = 0.006. NF63-64: top versus tip, p = <0.0001; top versus mid, p = 0.024). At NF57-58, when the knee starts participating in movement, it displays a similar low dominant frequency as the most rostral tail point, the top (**C**; tail tip versus knee, p = 0.029; tail mid versus knee, p = 0.118). Whereas, at NF63-64, time point of tail recession, the tail top most closely matches the low dominant frequency of the knee, followed by the tail tip (**D**; tail tip versus knee, p = 0.082; tail mid versus knee, p = 0.023). Mean power spectrum of oscillations at the tail top (circle, dark shade), mid (square, medium shade), and tip (triangle, light shade) for NF44-48 (**E**), NF52-55 (**F**), NF57-58 (**G**), NF59-62 (**H**), and NF63-64 (**I**) with low (0.9-4.5 Hz, dark gray) and high (4.5-20 Hz, light gray) frequency bins highlighted. From NF44-48 to NF59-62, all tail points display bimodal frequency spectra with a peak in the low and high frequency bins (**E-H**); while at NF63-64, they all show unimodal frequency spectra with only one low frequency peak (**I**). At NF44-48 (**E**), the top, mid and tip are similar in their frequency distribution; at all other stages (**F-I**), the power at the tail top is greater across the spectrum than the mid and tip.

J-Q. Range, coordination, and frequency of movement along the proximodistal axis of the hindlimb. When moving, the ankle and foot display an increased mean angle from NF57-58 to juvenile, while the mean angle of the hip first decreases until NF63-64 and then increases at juvenile stage (**J**. Hip: for NF57-58 to NF59-62 and NF63-64 versus juvenile, p = <0.0001; for NF57-58 versus juvenile, p = 0.0009. Ankle: NF57-58 to NF59-62, p = 0.0008; NF57-58 versus juvenile, p = <0.0001; NF59-62 versus NF63-64, p = 0.002; NF63-64 versus juvenile, p = 0.007. Foot: for NF57-58 to NF59-62, NF57-58 versus juvenile, NF59-62 versus NF63-64 and NF63-64 versus juvenile, p = <0.0001). The foot never reaches the same angle as the hip and ankle (**J**). From NF57-58 to NF59-62, only the range of ankle movement increases, while hip and foot remain unchanged. From NF59-62 to juvenile stage, all joints show a decrease in range of movement (**K**. Hip: for NF57-58 to juvenile and NF59-62 versus NF63-64, p = <0.0001; NF63-64 versus juvenile, p = 0.005. Ankle: for NF57-58 versus juvenile, NF59-62 versus NF63-64 and NF59-62 versus juvenile, p = <0.0001; for NF57-58 versus NF59-62 and NF63-64 versus juvenile, p = 0.0003. Foot: for NF57-58 versus juvenile, NF59-62 versus NF63-64 and NF59-62 versus juvenile, p = <0.0001; NF63-64 versus juvenile, p = 0.0005). Left-right coordination between knee, ankle and foot increases across metamorphosis, beginning with random bilateral movement at NF57-58 and gaining synchrony by NF63-64 (**L**; +1 = synchronous, 0 = random, -1 = alternating. Hip: NF57-58 versus NF59-62, p = 0.002; NF57-58 versus NF63-64, p = <0.0001; NF59-62 versus NF63-64, p = 0.0004. Ankle: NF57-58 versus NF59-62, p = 0.003; NF57-58 versus NF63-64, p = <0.0001; NF59-62 versus NF63-64, p = 0.004. Foot: NF57-58 versus NF63-64, p = <0.0001; NF59-62 versus NF63-64, p = 0.001). The foot never reaches the same level of bilateral synchronous movement as the hip and ankle (**L**). Mean power spectra of hip (circle, dark shade), knee (square, medium dark shade), ankle (triangle, medium shade) and foot (rhombus, light shade) oscillations from NF57-58 (**M**), NF59-62 (**N**), NF63-64 (**O**), to juvenile stage (**P**) show a similar unimodal distribution with only a low frequency peak. For all joints, the dominant low frequency (dotted black lines) increases across metamorphosis from ~1.5Hz to ~2.2Hz at NF63-64 (**M-P**). The amount of movement of the hip and foot in the low frequency bin, represented by the sum power, increases across metamorphosis reaching the peak at NF63-64 (**Q**. Hip: NF57-58 versus NF59-62, p = 0.001; for NF57-58 versus NF63-64 and NF59-62 versus NF63-64, p =

<0.0001. Foot: NF57-58 versus NF59-62, p = 0.002; for NF57-58 versus NF63-64 and NF59-62 versus NF63-64, p = <0.0001).
n = 172 animals for NF37-38; n = 47 animals for NF44-48; n = 24 animals for NF52-55, n = 11 animals for NF57-58, n = 13 animals for NF59-62, n = 8 animals for NF63-64, n = 13 animals for juvenile stage.

Figure S3. Motor neuron subtypes in developing *Xenopus* tadpoles, related to Figure 2.
A. Spinal cross sections of NF44-47 tadpoles showing motor neuron (Isl1/2 and Hb9), medial motor column (MMC; Lhx3) or lateral motor column (LMC; FoxP1) markers at the brachial level.
B. Spinal cross sections of NF44-47 tadpoles showing motor neuron (Isl1/2 and Hb9), medial motor column (MMC; Lhx3), lateral motor column (LMC; Raldh2) or preganglionic column (PGC; FoxP1, P-Smad) markers at the thoracic level.
C. A schematic showing separation of mouse limb motor neurons at the brachial level into a medial and lateral division, LMCm and LMCl, respectively, and pools innervating distinct muscle groups in the forelimb.
D-E. In NF54 tadpoles, the LMC is divided into LMCm and LMCl divisions (**D**) and motor pools (**E**) distinguishable by transcription factor expression.
F. In NF54 tadpoles, P-Smad and Isl1/2 co-staining marks a preganglionic column at the thoracic level.
G. LMC is not present in NF35 tadpoles as shown by Isl1/2 and Raldh2 co-staining. Shown is mean ± SEM (n = 4 animals).
H-J. Percentage of motor neurons belonging to each motor column in axial spinal cord at NF35-38 (**H**), limb (**I**) and thoracic (**J**) levels at NF44-47. Shown is mean ± SEM (n = 2–14 animals).
All images represent 15 µm cross sections.

Figure S4. Timeline of limb and spinal cell type development in *Xenopus laevis*, related to Figures 2, 4, and 6.
A. Schematic representation of the forelimb (FL) and hindlimb (HL) at NF48-57.
B. Immunostaining of motor neurons marked by Hb9 and motor columns marked by FoxP1 (lateral motor column, LMC) or Lhx3 (medial motor column, MMC) at the lumbar level.
C-D. Immunostaining of V1 interneurons marked by En1 and V1 subsets marked by FoxP1, FoxP2 or Pou6f2.
E-K. Quantification of the number of all motor neurons (**E**), MMC (**F**) or LMC (**G**) motor neurons, V1 interneurons (**H**), $V1^{FoxP2}$ (**I**), $V1^{FoxP2}$ (**J**) $V1^{Pou6f2}$ (**K**) at the lumbar level. Shown is mean ± SEM for n = 2 animals.
All images represent 15 µm cross sections. Scale bar, 50 µm. Drawings modified from Xenbase[118] and Xenopus illustrations © Natalya Zahn (2022)[117].

Figure S5. Expression of En1 is maintained in lineage-traced V1 interneurons during mouse development, related to Figures 4 and 6.
A. Lumbar cross section of *En1::Cre; RC.lsl.Sun1.sfGFP* e13.5 spinal cord showing immunodetection of En1 protein (red) in a subset of lineage-traced V1 interneurons (green)
B-C. Spatial distributions of the parental V1 population (green; **B**) and neurons actively expressing En1 (red; **C**).

Figure S6. V1 subtype diversity emergence during metamorphosis, related to Figure 5.
A-C. Spinal cross sections showing transcription factor expression at larval (**A**), free-swimming (**B**), and limb-circuit stages (**C**) of *Xenopus* development. Tadpole drawings adapted from Xenopus illustrations © Natalya Zahn (2022)[117].
D. Quantification of percentage of V1s expressing a given transcription factor in axial (NF35-38), thoracic (NF44-47 and NF54-55) or lumbar spinal cord (NF54). Shown is mean ± SEM for = 4–10 animals.
E-H. Quantification of percentage of V1s expressing a given transcription factor at the corresponding stages and levels shown in **A-C**. Shown is mean ± SEM for = 4–10 animals.
All images represent 15 µm cross sections.

Figure S7. Molecular and spatial organization of V1 subsets along rostrocaudal axis of frog and mouse spinal cord, related to Figure 6.
A-C. Immunoreactivity against V1 marker En1 (red) and subtype markers FoxP2 (green) and MafB (blue) at the brachial (**A**), thoracic (**B**), and lumbar (**C**) segment of the NF54-55 frog. The distribution of En1+ cells for each level is shown in **A'-C**'.
D. Number of V1s per spinal level (brachial, thoracic and lumbar) in the NF54-55 frog (black) and the P0 mouse (gray) per 15 µm ventral horn (mean ± SEM for n = 2–4 animals).
E. Percentage of V1s expressing a given subset transcription factor (TF) in the frog (black) and mouse (gray) thoracic spinal cord.
F. Fold change of the percentage of V1s co-expressing one TF (top, based on **E**) or two TFs (bottom) between the frog and mouse thoracic spinal cords. More than two enriched populations for frog (black) or mouse (gray) are indicated.
G. A ventral population (**G''**) of V1 interneurons (En1, green) co-expresses the Renshaw cell markers MafB (red) and Calbindin (blue) in the NF54-55 frog spinal cord, quantified in **G'**. Shown is mean ± SEM for n = 4 animals
H-Q. Spatial plots showing the distribution of V1 expressing a given TF at the thoracic (**H-Q**) and lumbar levels (**K'-Q'**) in the frog (top row) and the mouse (bottom row).

Figure S8. FoxP1 knockout affects motor neuron subtype but not V1 specification or motor neuron limb projections, related to Figure 7.
A-B. Generation of bilateral FoxP1 CRISPR mutant frogs. Injection of FoxP1 sgRNA and Cas9 protein at one cell stage (**A**). Resulting mutants (**B** right) largely lacked FoxP1 (red) and Raldh2 (green) immunoreactivity as compared to wiltype (**B** left). Isl1/2-positive (blue) motor neurons were present in both conditions (**B**).
C-D. Quantification of bilateral FoxP1 mutants showed that FoxP1$^+$ (**C**) and Raldh2$^+$ (LMC, **D**) motor neurons were decreased at all spinal levels at NF54 ($p < 0.05$ for all levels except for Raldh2 at thoracic levels). Shown are mean ± SEM (n = 6 animals) per 15 µm ventral horn.
E-F. Genomic characterization of unilateral and bilateral FoxP1 CRISPR mutant animals. TIDE analysis reveals high efficiency of FoxP1 sgRNA in generating bilateral mutant animals at NF44-48 (**E**; WT vs mutant, $p = 0.024$, n = 3 for WT and n = 6 for FoxP1 animals), as well as unilateral mutant animals at juvenile stage (**F**; n = 2 for WT and n = 4 for FoxP1 animals).
G-J. Profiling of other spinal neuron types in FoxP1 mutant. Quantification of MMC (Hb9$^+$Lhx3$^+$, **G**) and V1 (En1$^+$, **H**) neurons on the mutant and uninjected side of the spinal cord

at all spinal levels. Shown are mean ± SEM (n = 3–6 animals) per 15 µm ventral horn. $V1^{1TF}$ (**I**) and $V1^{2TF}$ (**J**) subtypes are largely unaffected in unilateral FoxP1 mutants at NF54-55. Shown are mean ± SEM (n = 3–6 animals) per 15 µm ventral horn.

K-L. Retrograde labeling with rhodamine dextran (RhD, red) labels LMC motor neurons (FoxP1+, blue; Raldh2+, green; Isl1/2+, white) that project to the hindlimb in both wildtype **(L**) and unilateral FoxP1 CRISPR (**M**) mutant animals. Scale bar, 40 µm.

Figure S9. Extended analysis of the effect of FoxP1 loss-of-function on limb- and tail-based locomotion, related to Figure 7.

A-F. Unilateral FoxP1 CRISPR mutant frogs display reduced locomotion at juvenile stage. Trajectories of the distance traveled by an exemplary WT (**A** left) and unilateral FoxP1 CRISPR animals (**A** right) show different patterns of movement. FoxP1 mutants edge track as WT (**A** left), but move with less consistent direction (**A** right). Scale bar in **A** indicates the number of times the animal was present in a specific area of the dish from no time (10^0 frames, yellow) to many times (10^3 frames, blue). Quantification of overall movement of FoxP1 mutant animals shows that they move for less time (**B**; WT versus FoxP1 ½ CRISPR, p = 0.036) with shorter trajectory length (**C**; WT versus FoxP1 ½ CRISPR, p = 0.024) and less acceleration (**E**; WT versus FoxP1 ½ CRISPR, p = 0.002). Mutants however employ similar speed to WT (**D**). Unilateral FoxP1 CRISPR frogs also turn more than WT, with no difference between turning towards or away from the mutant side (**F**; for WT + versus FoxP1 ½ CRISPR +, WT + versus FoxP1 ½ CRISPR -, WT - versus FoxP1 ½ CRISPR + and for WT - versus FoxP1 ½ CRISPR +, p = <0.0001). n = 13 for WT, n = 14 for unilateral FoxP1 CRISPR.

G-I. Loss of range, coordination and amount of movement along the rostrocaudal axis of the FoxP1 mutant hindlimb. Quantification of mean angle of the mutant hip, ankle and foot show a different position than WT when moving (**G**. Hip, ankle and foot: WT L versus FoxP1 ½ CRISPR, WT R versus FoxP1 ½ CRISPR and uninjected versus FoxP1 ½ CRISPR, p = <0.0001). Left-right coordination between hip, ankle and foot joints is lost in FoxP1 CRISPR animals (**H**; +1 = bilateral synchronous, 0 = random, -1 = alternate synchronous. Hip, ankle and foot: WT versus FoxP1 ½ CRISPR, p = <0.0001). At the hip, ankle and foot joints, the amount of movement in the low frequency bin (0.9-4.5 Hz), represented by the sum power, is reduced for the FoxP1 CRISPR mutant limb compared to WT hindlimbs (**I**. Hip: WT L versus FoxP1 ½ CRISPR, p = 0.005; WT R versus FoxP1 ½ CRISPR, p = 0.065; uninjected versus FoxP1 ½ CRISPR, p = 0.032. Ankle: WT L versus FoxP1 ½ CRISPR, p = 0.002; WT R versus FoxP1 ½ CRISPR, p = 0.002. Foot: WT L versus FoxP1 ½ CRISPR, p = 0.013; WT R versus FoxP1 ½ CRISPR, p = 0.002; uninjected versus FoxP1 ½ CRISPR, p = 0.005) n = 13 for WT, n = 14 for unilateral FoxP1 CRISPR.

J-P. Bilateral FoxP1 loss-of-function in NF44-48 does not affect tadpole locomotion. Trajectories of the distance traveled by an exemplary WT (left) and bilateral FoxP1 CRISPR animals (right) show similar patterns of movement (**J top**). Scale bar in **J top** indicates the number of times the animal was present in a specific area of the dish from no time (10^0 frames, yellow) to many times (10^3 frames, blue). SLEAP skeleton (yellow) superimposed on WT (left) and bilateral FoxP1 CRISPR (right) tadpoles at NF44-48 with PCA plots representing the position of the tail and its range of movement during 256 random frames (**J bottom**; tail top, dark blue; tail mid, blue; tail tip, light blue). Scale bar in **J bottom** indicates the color-code of the first principal component of variation of the aligned tail positions. Bilateral FoxP1 CRISPR animals move for comparable time (**K**) and distance (**L**) to WT, employing similar speed (**M**), acceleration (**N**), and turning (**O**). Quantification of the range of the tail tip (**J**, light blue)

movement shows similar displacement to WT (**P**). n = 47 for WT, n = 39 for bilateral FoxP1 CRISPR.

Figure S10. Extended analysis of the effect of En1 loss-of-function on tail and limb movement in tadpoles and frogs, related to Figure 8.

A-F. En1 mutant tadpoles have less and slower locomotion at NF44-48 with increased range of tail movement. Trajectories of the distance traveled by an exemplary WT (**A**, left) and bilateral En1 CRISPR animals (**A**, right) show that mutant animals swim in circles and explore less of the dish (**A**). Scale bar in **A top** indicates the number of times the animal was present in a specific area of the dish from no time (10^0 frames, yellow) to many times (10^3 frames, blue). SLEAP skeleton (yellow) superimposed on WT (left) and bilateral En1 CRISPR (right) tadpoles at NF44-48 with PCA plots representing the position of the tail and its range of movement during 256 random frames (**A bottom**; tail top, dark blue; tail mid, blue; tail tip, light blue). Scale bar in **A bottom** indicates the color-code of the first principal component of variation of the aligned tail positions. Bilateral En1 CRISPR animals move for less time (**B**; WT versus En1 CRISPR, p = 0.022) with shorter distance traveled (**C**; WT versus En1 CRISPR, p = 0.0006) and employ slower speed (**D**; WT versus En1 CRISPR, p = <0.0001) and acceleration (**E**; WT versus En1 CRISPR, p = 0.002), while turning more than WT (**F**; WT versus En1 CRISPR, p = <0.0001). Quantification of the range of the tail tip (**A**, light blue) movement in bilateral En1 CRISPR mutant animals shows increased range in bilateral En1 CRISPR mutants compared to WT (**G**). n = 47 for WT and n = 37 for bilateral En1 CRISPR.

H-L. Loss of high frequency and gain of low frequency movement in En1 CRISPR tadpoles at NF44-48. Mean power spectrum of the tail tip oscillation shows a bimodal distribution for WT, with two peaks in the low and high frequency bin, and a unimodal distribution for bilateral En1 CRISPR animals, with only one peak in the low frequency bin for (**H**; low frequency bin, 0.9-4.5 Hz, dark gray; high frequency bin, 4.5-20 Hz, light gray). Bilateral En1 CRISPR mutant animals increase low frequency movement, gaining sum power in the low frequency bin (**I**; WT vs En1 CRISPR, p = <0.0001) and losing power in the high frequency bin (**K**; WT vs En1 CRISPR, p = 0.003). This loss is also captured by the flattening of the curve in the high frequency bin for the mutants (**H**). En1 CRISPR bilateral mutant tadpoles also have a decreased dominant low frequency (**J**; WT vs En1 CRISPR, p = 0.002) and no change in dominant high frequency (**L**). Notably, only a third of the bilateral En1 CRISPR mutant tadpoles even generate a dominant high frequency. n = 47 for WT and n = 37 for bilateral En1 CRISPR.

M-R. Overall locomotion is not affected in En1 CRISPR mutant frogs. Trajectories of the distance traveled by an exemplary WT (**M** left) and unilateral En1 CRISPR animals (**M** right) show similar patterns of movement with dish edge tracking. Scale bar in **M** indicates the number of times the animal was present in a specific area of the dish from no time (10^0 frames, yellow) to many times (10^3 frames, blue). Unilateral En1 CRISPR animals move for comparable time (**N**), distances (**O**) and employ similar speed (**P**) and acceleration (**Q**), while turning more than WT (**R**; WT versus En1 ½ CRISPR, p = 0.015). n = 13 for WT, n = 8 for unilateral En1 CRISPR.

S-U. Neither range nor coordination of movement are affected in En1 mutant frogs. While moving, the displacement of the hip, knee and ankle of unilateral En1 CRISPR mutant animals is comparable to WT animals (**S**). The range of movement of the hip and ankle is similarly unaffected; only the foot shows a higher range of displacement in En1 mutants compared to WT animals (**T**. Foot: WT versus En1 ½ CRISPR, p = <0.0001). Left-right coordination between hip, ankle and foot joints is also unaffected in unilateral En1 CRISPR

(**U**; +1 = synchronous, 0 = random, -1 = alternating). n = 13 for WT, n = 8 for unilateral En1 CRISPR.

V-W. Lower dominant frequency in En1 CRISPR mutant frogs at all hindlimb joints. At the hip, ankle and foot joints, the amount of movement, represented by the sum power, in the low frequency bin (0.9-4.5 Hz) is similar between WT and unilateral En1 CRISPR animals (**V**). However, the dominant frequency of the hip, ankle and foot is lower in mutants compared to WT animals (**W**. Hip: WT versus En1 ½ CRISPR, p = 0.039. Ankle: WT versus En1 ½ CRISPR, p = 0.043. Foot: WT versus En1 ½ CRISPR, p = 0.029). n = 13 for WT, n = 8 for unilateral En1 CRISPR.

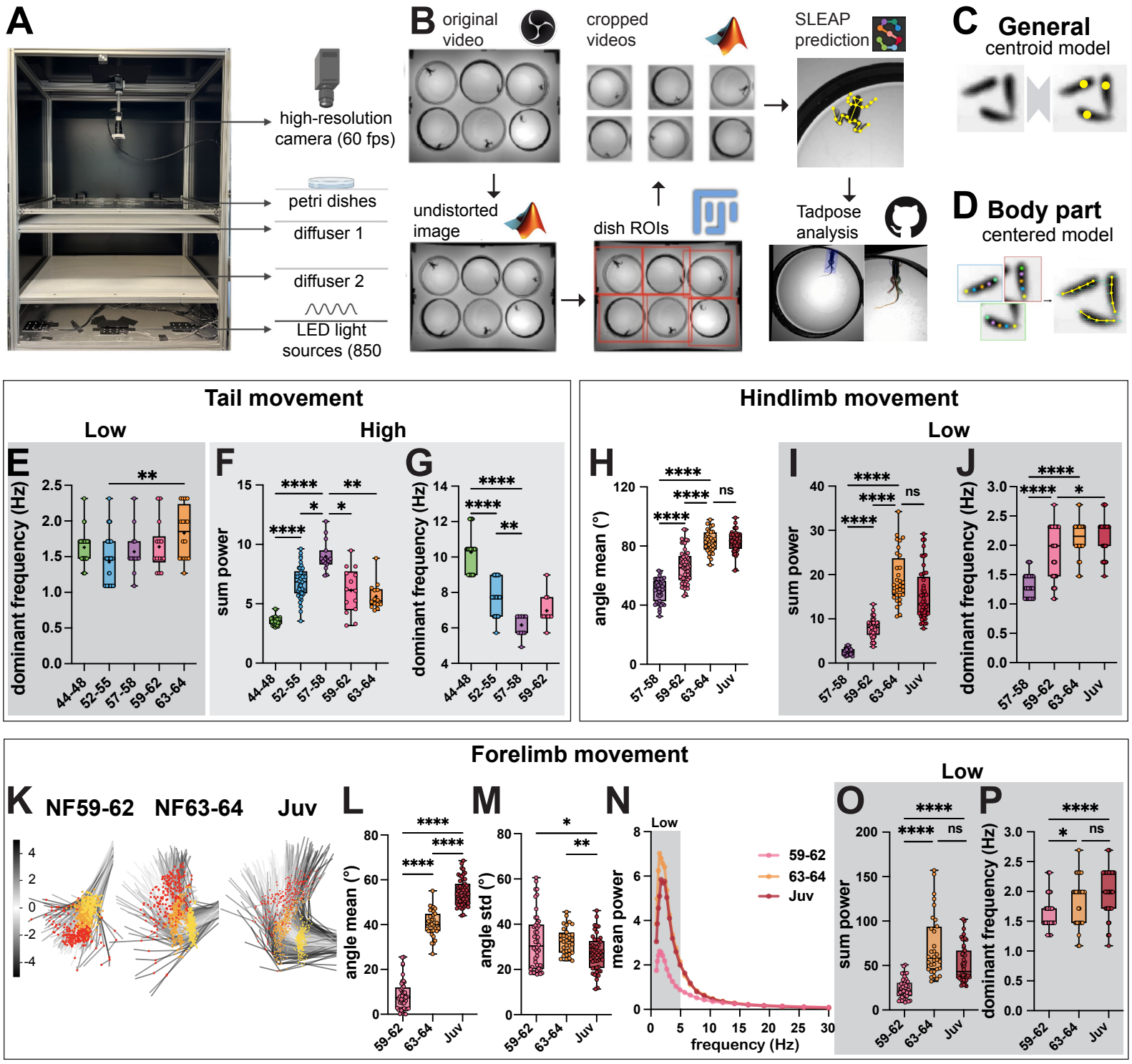
A
high-resolution camera (60 fps)
petri dishes
diffuser 1
diffuser 2
LED light sources (850
B
original video
undistorted image
dish ROIs
cropped videos
SLEAP prediction
Tadpose analysis
C General
centroid model
D Body part
centered model
Tail movement
Low
High
E
F
G
dominant frequency (Hz)
sum power
dominant frequency (Hz)
44-48
52-55
57-58
59-62
63-64
Hindlimb movement
Low
H
I
J
angle mean (°)
sum power
dominant frequency (Hz)
57-58
59-62
63-64
Juv
Forelimb movement
K
NF59-62
NF63-64
Juv
L
M
N
O
P
angle mean (°)
angle std (°)
mean power
frequency (Hz)
Low
59-62
63-64
Juv
sum power
dominant frequency (Hz)
ns

Figure S1

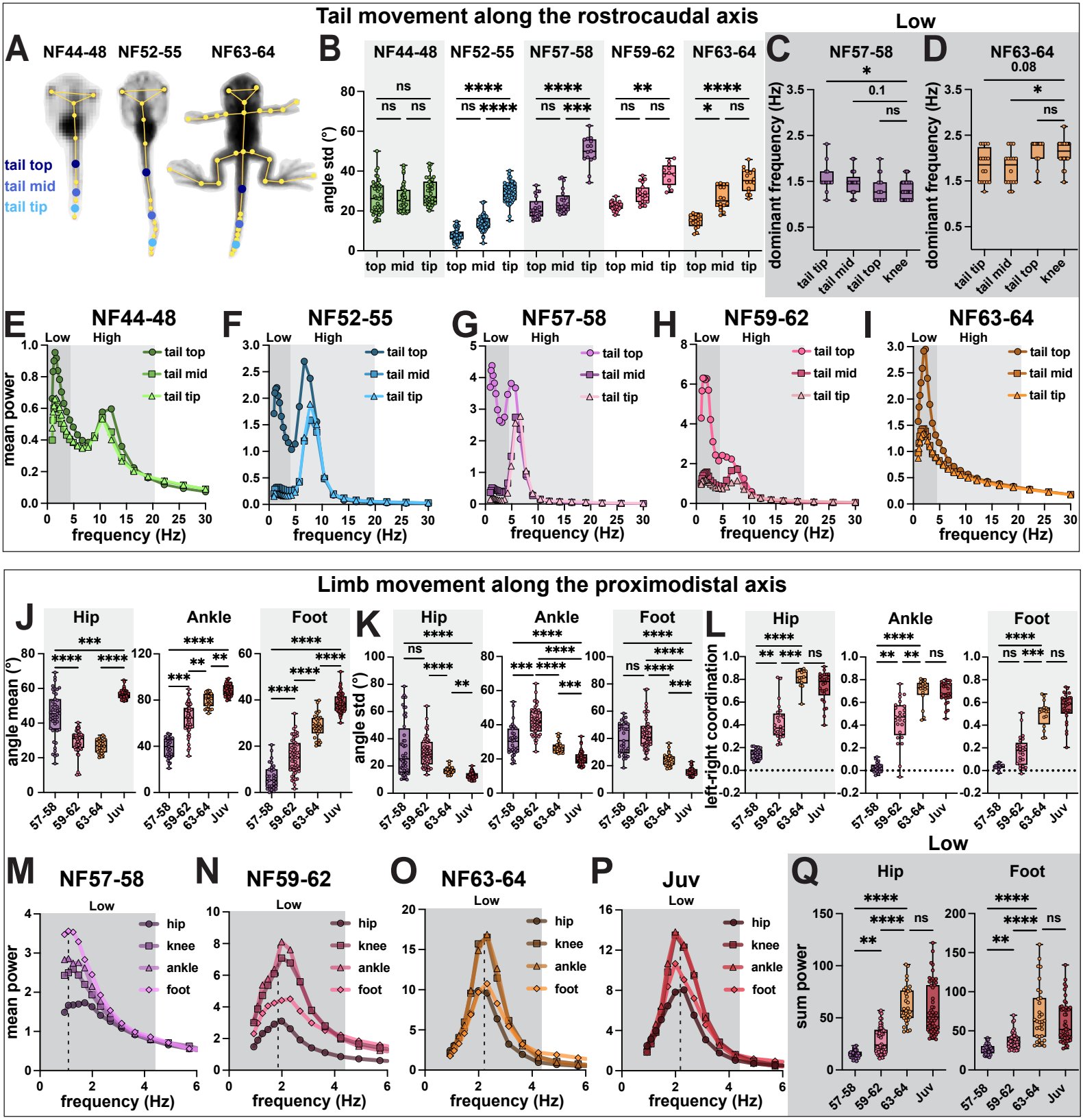
Tail movement along the rostrocaudal axis
A
NF44-48
NF52-55
NF63-64
tail top
tail mid
tail tip
B
NF44-48
NF52-55
NF57-58
NF59-62
NF63-64
angle std (°)
top mid tip
Low
C
NF57-58
D
NF63-64
dominant frequency (Hz)
tail tip
tail mid
tail top
knee
E
NF44-48
F
NF52-55
G
NF57-58
H
NF59-62
I
NF63-64
Low
High
mean power
frequency (Hz)
Limb movement along the proximodistal axis
J
Hip
Ankle
Foot
angle mean (°)
K
angle std (°)
L
left-right coordination
57-58
59-62
63-64
Juv
M
NF57-58
N
NF59-62
O
NF63-64
P
Juv
hip
knee
ankle
foot
Q
sum power

Figure S2

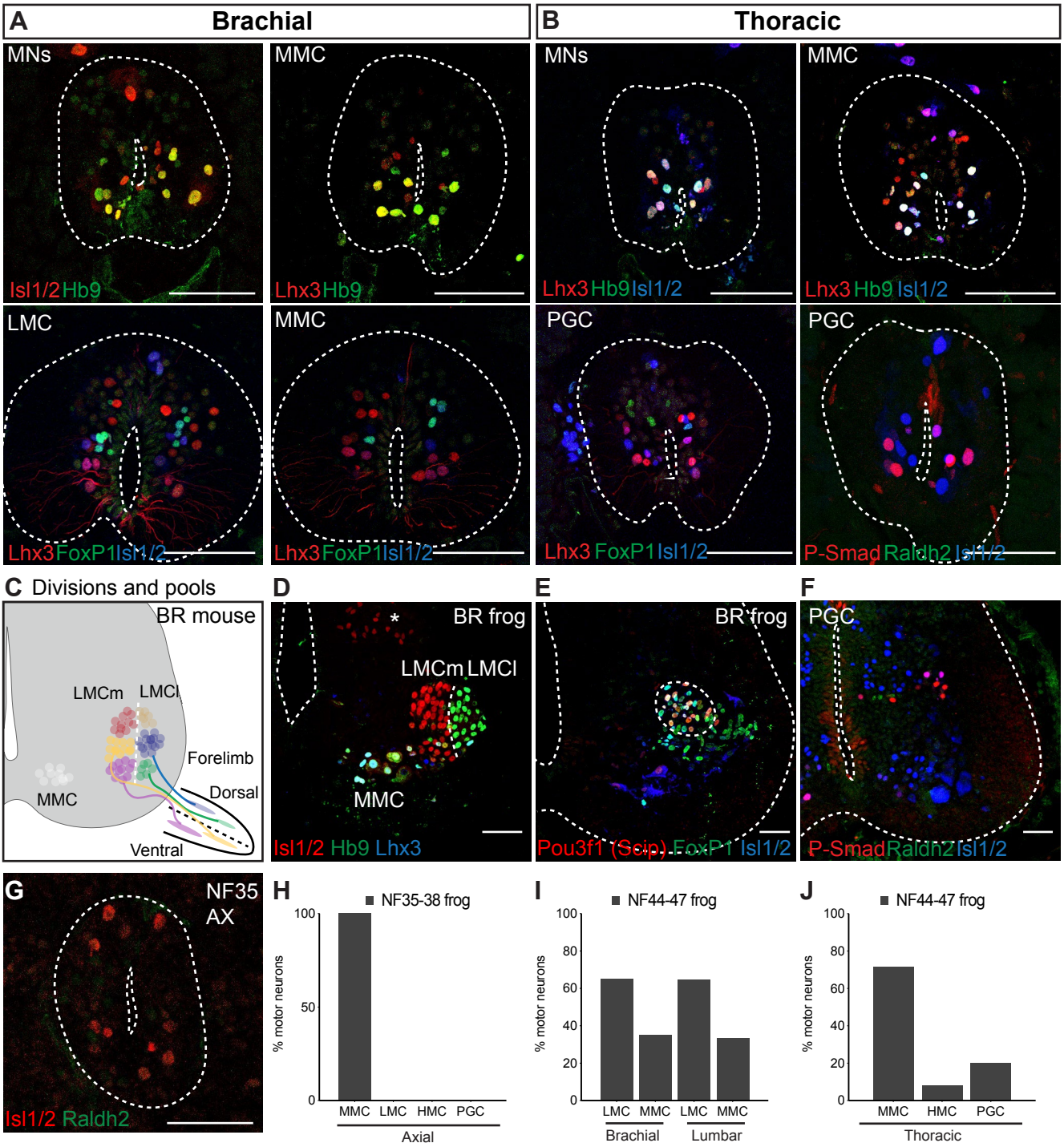
A
Brachial
B
Thoracic
MNs
Isl1/2 Hb9
MMC
Lhx3 Hb9
MNs
Lhx3 Hb9 Isl1/2
MMC
Lhx3 Hb9 Isl1/2
LMC
Lhx3 FoxP1 Isl1/2
MMC
Lhx3 FoxP1 Isl1/2
PGC
Lhx3 FoxP1 Isl1/2
PGC
P-Smad Raldh2 Isl1/2
C Divisions and pools
BR mouse
LMCm
LMCl
Forelimb
Dorsal
MMC
Ventral
D
BR frog
LMCm LMCl
MMC
Isl1/2 Hb9 Lhx3
E
BR frog
Pou3f1 (Scip) FoxP1 Isl1/2
F
PGC
P-Smad Raldh2 Isl1/2
G
NF35
AX
Isl1/2 Raldh2
H
NF35-38 frog
% motor neurons
100
50
0
MMC LMC HMC PGC
Axial
I
NF44-47 frog
% motor neurons
100
80
60
40
20
0
LMC MMC LMC MMC
Brachial
Lumbar
J
NF44-47 frog
% motor neurons
100
80
60
40
20
0
MMC HMC PGC
Thoracic

Figure S3

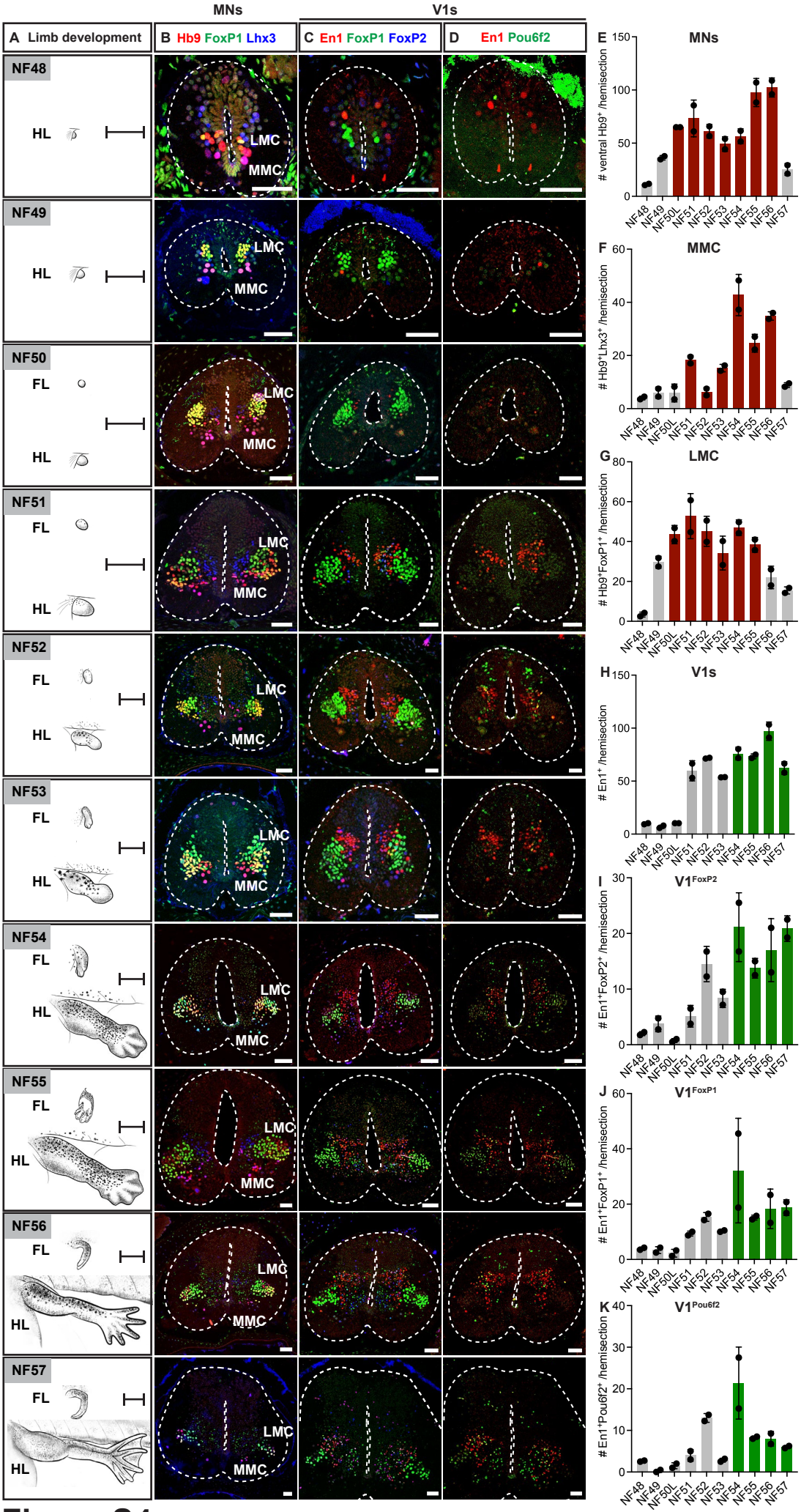
MNs
V1s
A Limb development
B Hb9 FoxP1 Lhx3
C En1 FoxP1 FoxP2
D En1 Pou6f2
NF48
NF49
NF50
NF51
NF52
NF53
NF54
NF55
NF56
NF57
HL
FL
LMC
MMC
E MNs
ventral Hb9+ /hemisection
F MMC
Hb9+Lhx3+ /hemisection
G LMC
Hb9+FoxP1+ /hemisection
H V1s
En1+ /hemisection
I V1FoxP2
En1+FoxP2+ /hemisection
J V1FoxP1
En1+FoxP1+ /hemisection
K V1Pou6f2
En1+Pou6f2+ /hemisection
NF48 NF49 NF50L NF51 NF52 NF53 NF54 NF55 NF56 NF57

Figure S4

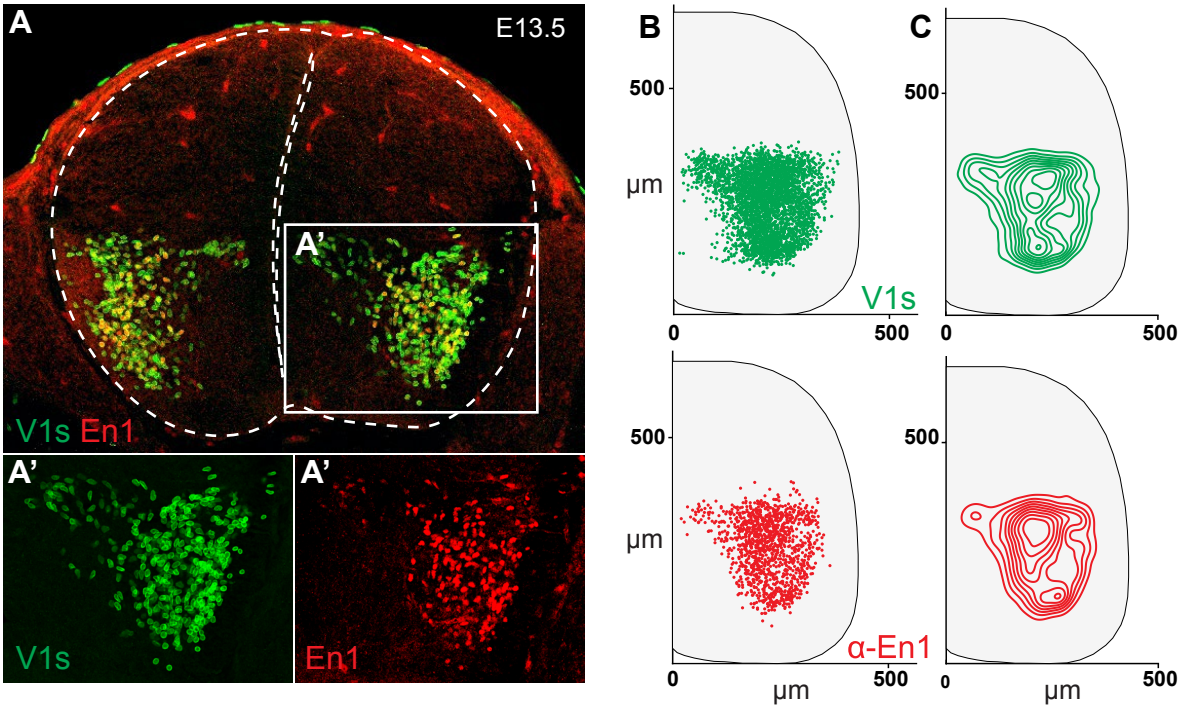
A
E13.5
A'
V1s En1
A'
V1s
A'
En1
B
C
500
µm
V1s
0
500
500
µm
α-En1
0
µm
500
0
500
µm

Figure S5

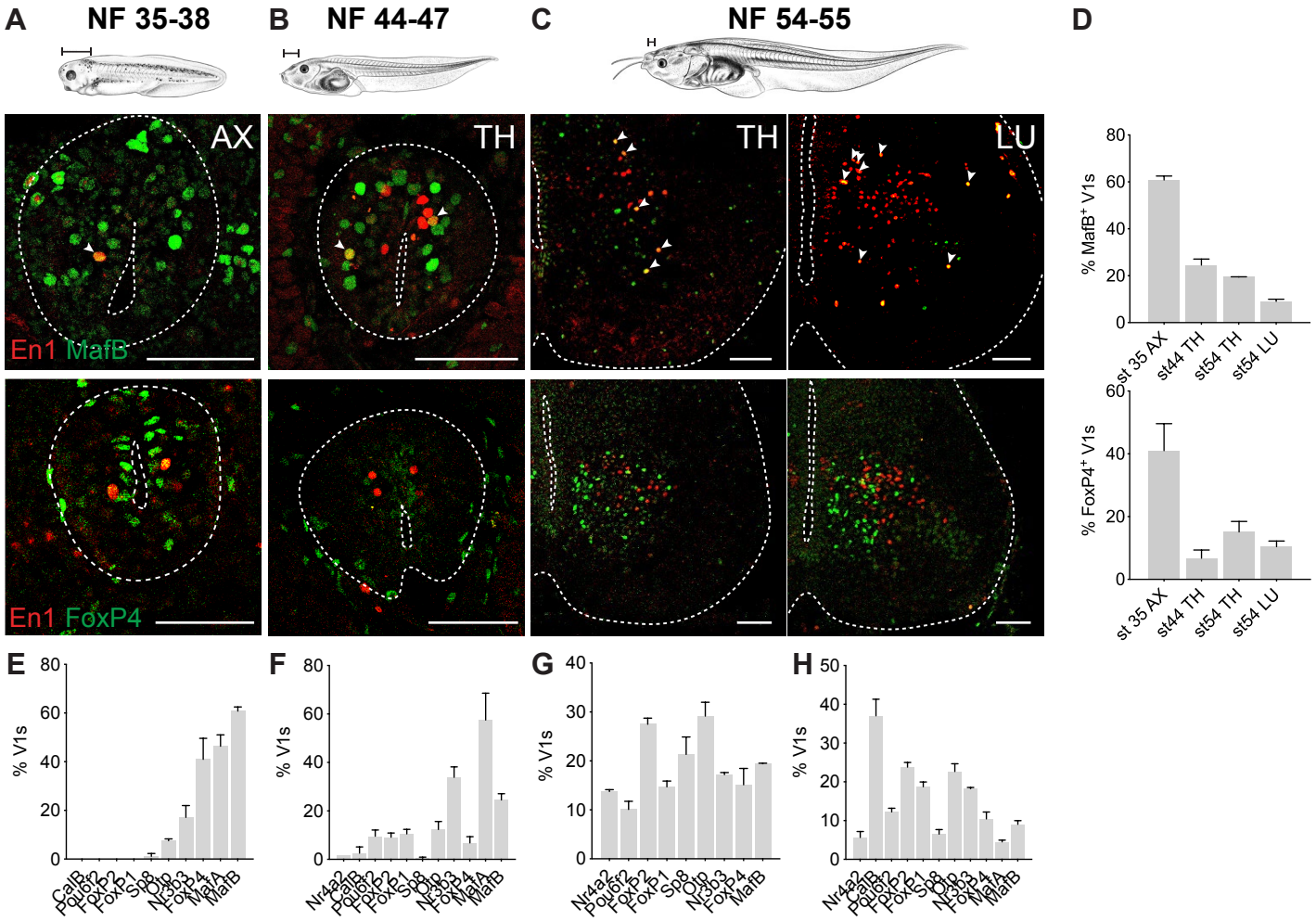
A
NF 35-38
B
NF 44-47
C
NF 54-55
D
AX
TH
TH
LU
En1 MafB
En1 FoxP4
% MafB+ V1s
% FoxP4+ V1s
st 35 AX
st44 TH
st54 TH
st54 LU
E
F
G
H
% V1s
CalB
Pou6f2
FoxP2
FoxP1
Sp8
Otp
Nr3b3
FoxP4
MafA
MafB
Nr4a2

Figure S6

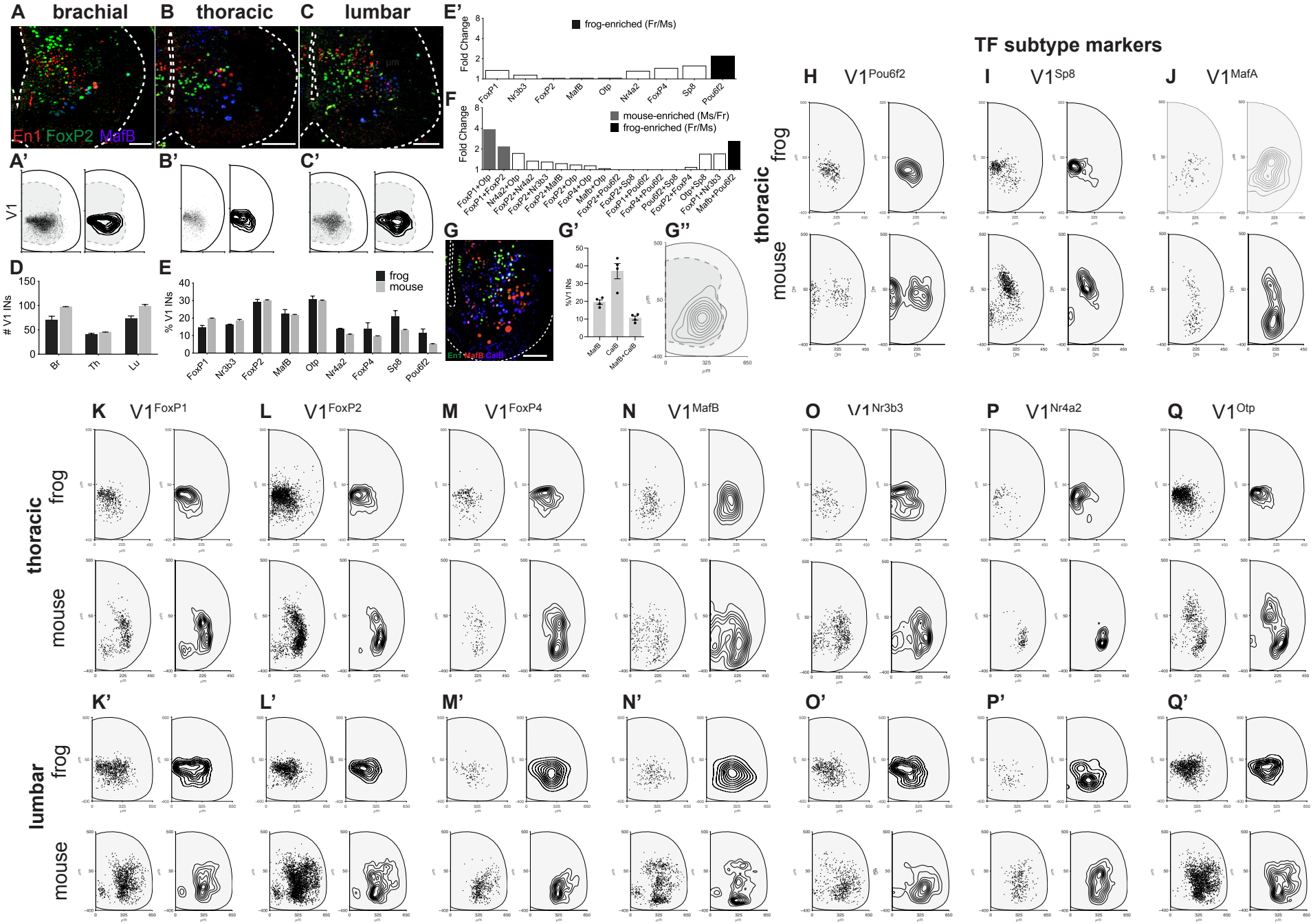
A brachial
B thoracic
C lumbar
En1 FoxP2 MafB
A'
B'
C'
V1
D
V1 INs
Br
Th
Lu
E
% V1 INs
frog
mouse
FoxP1
Nr3b3
FoxP2
MafB
Otp
Nr4a2
FoxP4
Sp8
Pou6f2
E'
frog-enriched (Fr/Ms)
Fold Change
F
mouse-enriched (Ms/Fr)
frog-enriched (Fr/Ms)
FoxP1+Otp
FoxP1+FoxP2
Nr4a2+Otp
FoxP2+Nr4a2
FoxP2+Nr3b3
FoxP2+MafB
FoxP2+Otp
FoxP4+Otp
MafB+Otp
FoxP2+Pou6f2
FoxP2+Sp8
FoxP1+Pou6f2
FoxP4+Pou6f2
Pou6f2+Sp8
Pou6f2+FoxP4
Otp+Sp8
FoxP1+Nr3b3
MafB+Pou6f2
G
En1 MafB CalB
G'
% V1 INs
MafB
CalB
MafB+CalB
G''
TF subtype markers
H V1Pou6f2
I V1Sp8
J V1MafA
thoracic
frog
mouse
K V1FoxP1
L V1FoxP2
M V1FoxP4
N V1MafB
O V1Nr3b3
P V1Nr4a2
Q V1Otp
lumbar
K'
L'
M'
N'
O'
P'
Q'

Figure S7

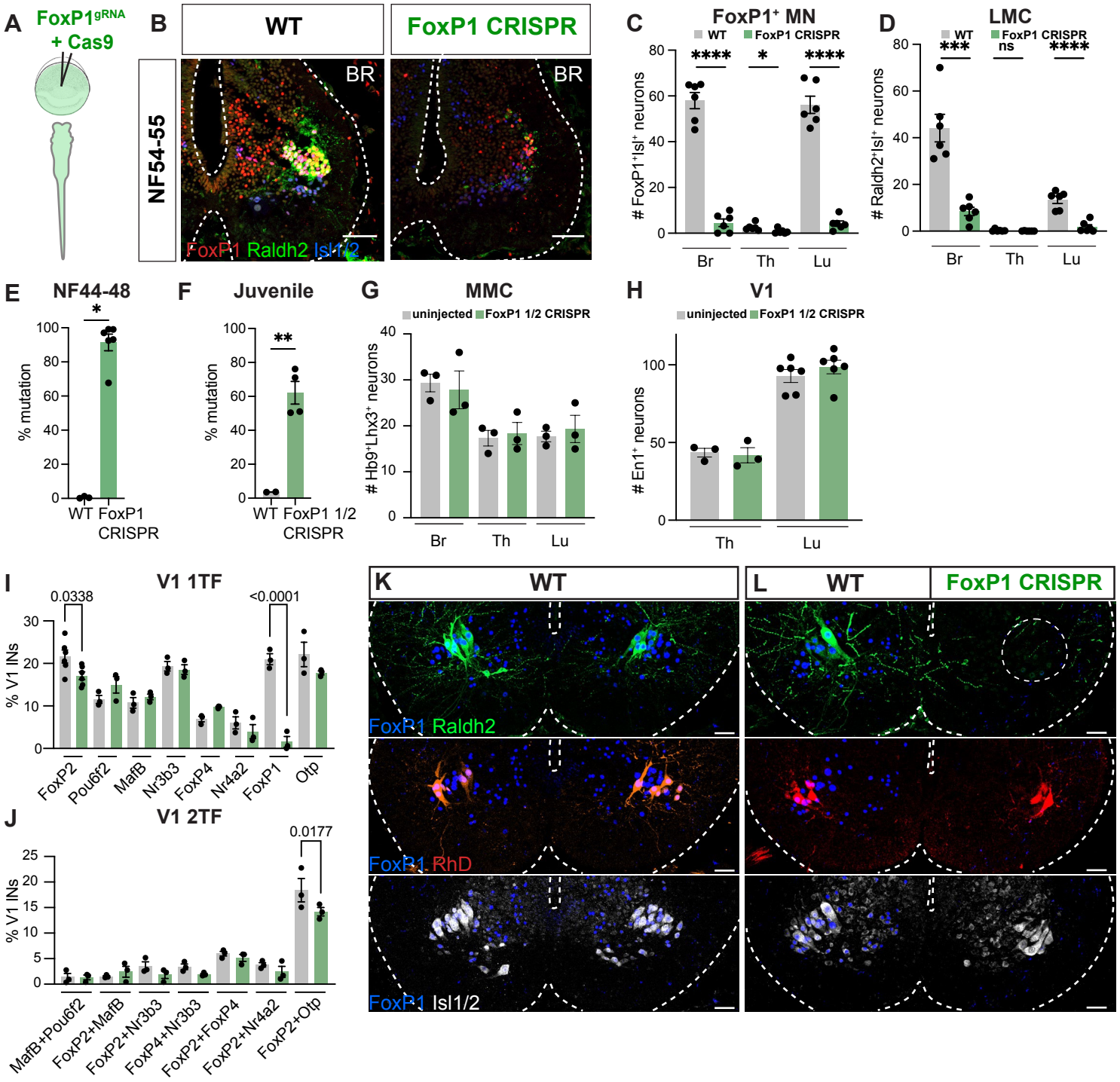
A
FoxP1gRNA + Cas9
B
WT
FoxP1 CRISPR
NF54-55
BR
FoxP1 Raldh2 Isl1/2
C
FoxP1+ MN
WT
FoxP1 CRISPR
FoxP1+Isl+ neurons
****
*
****
Br
Th
Lu
D
LMC
***
ns
****
Raldh2+Isl+ neurons
E
NF44-48
% mutation
WT
FoxP1 CRISPR
F
Juvenile
**
WT
FoxP1 1/2 CRISPR
G
MMC
uninjected
FoxP1 1/2 CRISPR
Hb9+Lhx3+ neurons
H
V1
En1+ neurons
I
V1 1TF
0.0338
<0.0001
% V1 INs
FoxP2
Pou6f2
MafB
Nr3b3
FoxP4
Nr4a2
FoxP1
Otp
J
V1 2TF
0.0177
MafB+Pou6f2
FoxP2+MafB
FoxP2+Nr3b3
FoxP4+Nr3b3
FoxP2+FoxP4
FoxP2+Nr4a2
FoxP2+Otp
K
WT
L
WT
FoxP1 CRISPR
FoxP1 Raldh2
FoxP1 RhD
FoxP1 Isl1/2

Figure S8

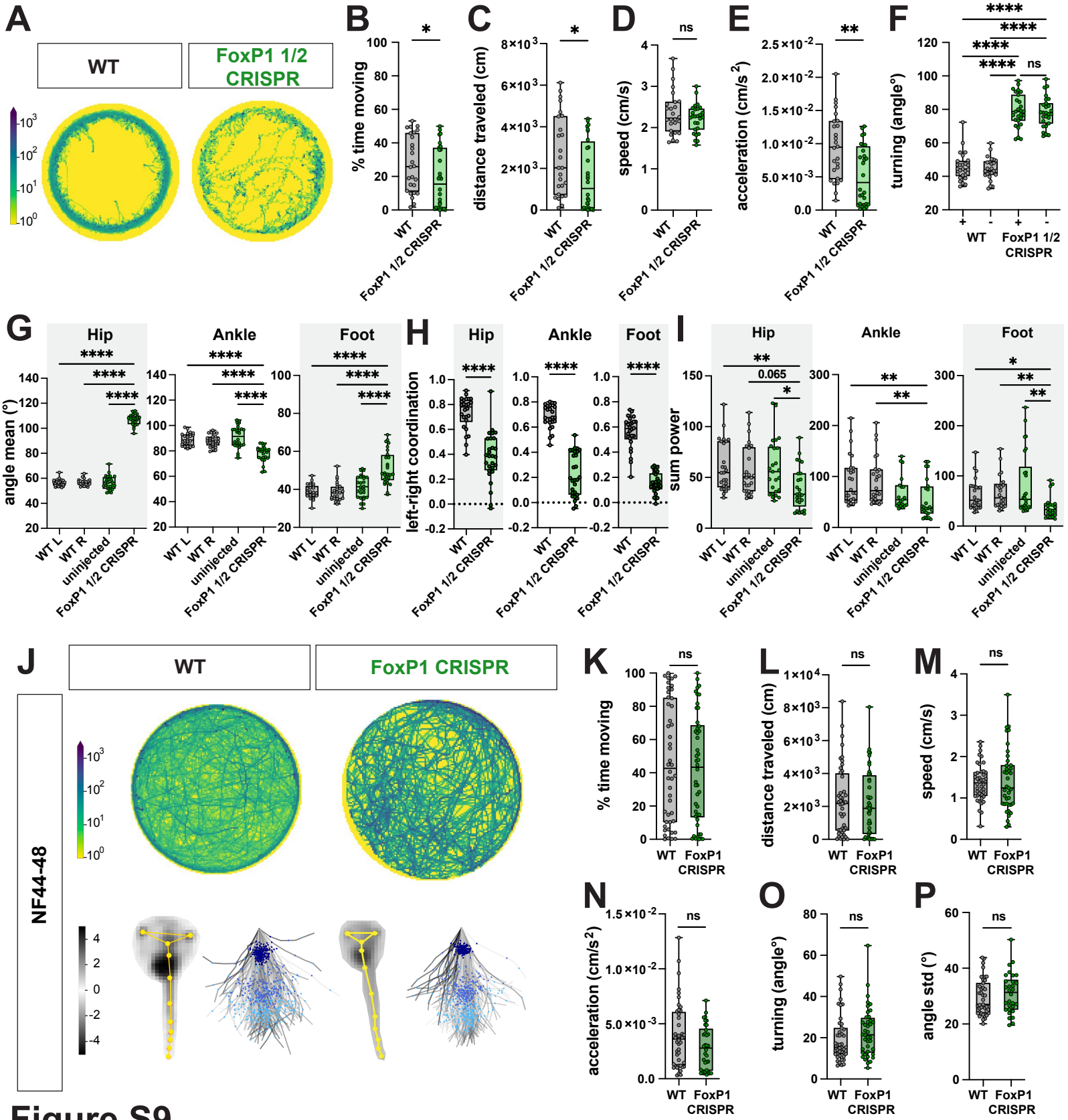
A
WT
FoxP1 1/2 CRISPR
B
% time moving
C
distance traveled (cm)
D
speed (cm/s)
E
acceleration (cm/s²)
F
turning (angle°)
WT
FoxP1 1/2 CRISPR
G
Hip
Ankle
Foot
angle mean (°)
H
left-right coordination
I
sum power
WT L
WT R
uninjected
FoxP1 1/2 CRISPR
J
WT
FoxP1 CRISPR
NF44-48
K
% time moving
L
distance traveled (cm)
M
speed (cm/s)
N
acceleration (cm/s²)
O
turning (angle°)
P
angle std (°)
WT
FoxP1 CRISPR

Figure S9

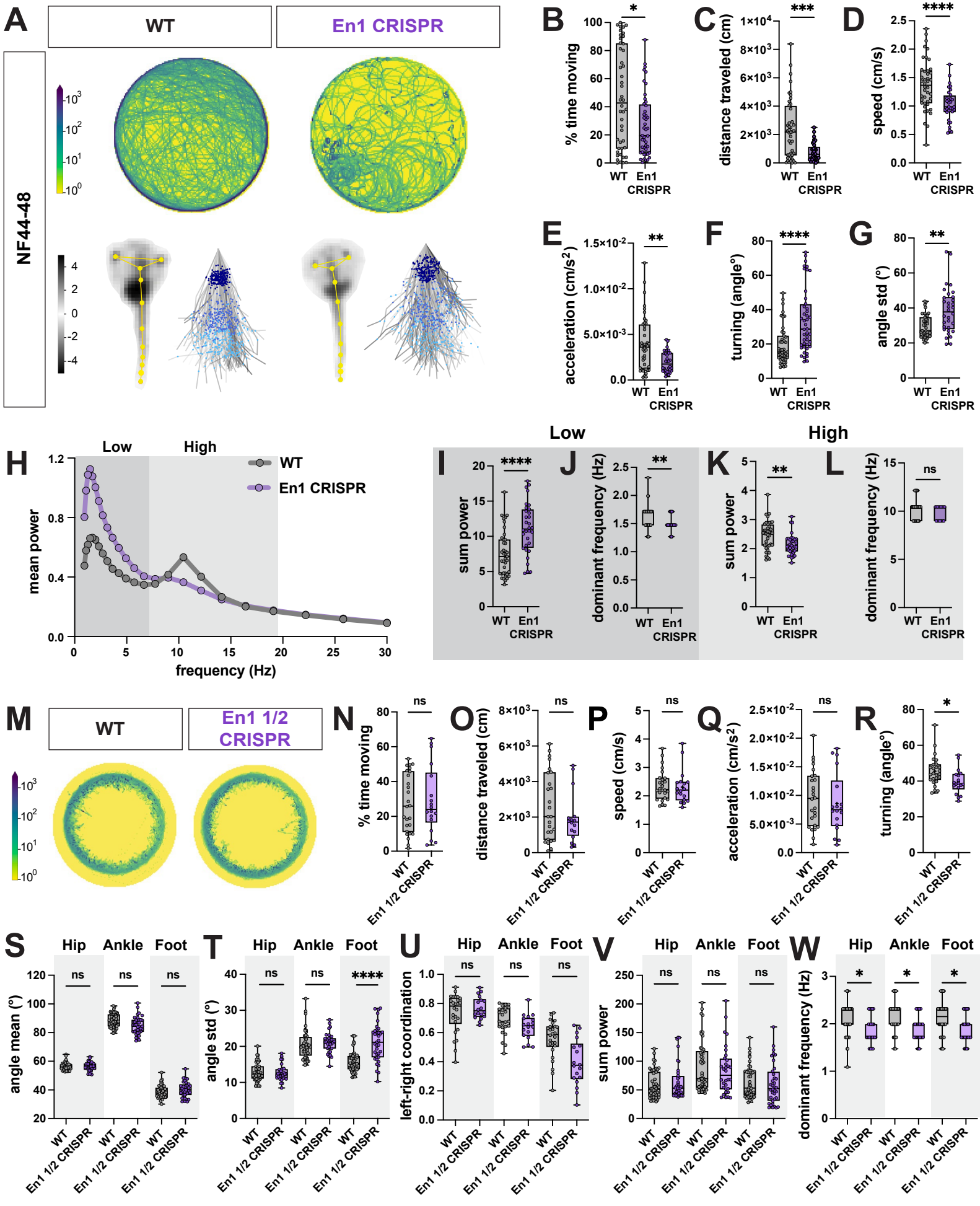
A
WT
En1 CRISPR
NF44-48
B
% time moving
C
distance traveled (cm)
D
speed (cm/s)
E
acceleration (cm/s²)
F
turning (angle°)
G
angle std (°)
WT
En1 CRISPR
H
Low
High
mean power
frequency (Hz)
I
sum power
J
dominant frequency (Hz)
K
sum power
L
dominant frequency (Hz)
M
WT
En1 1/2 CRISPR
N
% time moving
O
distance traveled (cm)
P
speed (cm/s)
Q
acceleration (cm/s²)
R
turning (angle°)
S
angle mean (°)
T
angle std (°)
U
left-right coordination
V
sum power
W
dominant frequency (Hz)
Hip
Ankle
Foot
ns

Figure S10

Number	Name	Sequence	Purpose	Source
SP533	GFP_for	GCACGACTTCTTCAAGTCCGCCAT	Genotyping	IDT
SP534	GFP_rev2	GCGGATCTTGAAGTTCACCTTGAT	Genotyping	IDT
SP154	FoxP1_gRNA1_for	GGAGTGAGGGCATCATTTGT	Genotyping	IDT
SP155	FoxP1_gRNA1_rev	GGTAAGGGAGGGAGGTAACG	Genotyping/TIDE	IDT
SP01	En1_gRNA4_for	GGAGAATTGTTGGAAGGGAGA	Genotyping	IDT
SP02	En1_gRNA4_rev	AGTAGATTTCCCTGTTGCTGG	Genotyping/TIDE	IDT

Table S1: Primer sequences used for PCR genotyping and TIDE analysis.

Target gene	Name	Sequence	Purpose	Source
FoxP1	FoxP1_gRNA1	ACTTGTGTAGACTAAGATTATGG	generating bilateral and unilateral mutants	Synthego
En1	En1_gRNA4	GCTCAGCAGTGAAGGCTGTTCGG	generating bilateral and unilateral mutants	Synthego

Table S2: Guide RNA sequences used to generate CRISPR mutants.

Metrics						
Model	**Stage bin**	**Average distance**	**Visual recall**	**Visual Precision**	**OKS**	**mPCK**
Centroid model	NF37-38	1.03709	1	1	0.94186	0.94395
	NF44-48	6.95001	1	1	0.54758	0.8125
	NF52-55	0.00001	1	1	0.92079	0.85714
	NF57-58	0.00001	1	1	0.47525	1
	NF59-62	0.00001	1	1	0.32673	1
	NF63-64	0.00001	1	1	0.76238	1
	Juvenile	0.00001	1	1	0.62376	1
Centered model	NF37-38	2.97621	0.98443	0.99751	0.34501	0.86163
	NF44-48	6.1345	0.93077	0.97059	0.10264	0.71244
	NF52-55	3.44924	0.93722	0.99524	0.33574	0.68918
	NF57-58	3.17561	0.94041	0.95863	0.5896	0.66311
	NF59-62	2.6415	0.99508	0.95997	0.77718	0.68521
	NF63-64	1.71405	0.99754	0.98901	0.81273	0.87478
	Juvenile	2.14075	0.99657	0.97865	0.88478	0.81674

Table S3: Metrics of the behavioral tracking models.

Gene to amplify	Step	PCR temperature	Time	Cycles
FoxP1	Initial denaturation	98 °C	30s	1
	Denaturation	98 °C	5s	32
	Annealing	57.7 - 63.3°C	5s	
	Extension	72 °C	10s	
	Final extension	72 °C	60s	1
	Storage	12 °C	∞	Storage
En1	Initial denaturation	98 °C	30s	1
	Denaturation	98 °C	5s	32
	Annealing	57.3 - 63.3°C	5s	
	Extension	72 °C	10s	
	Final extension	72 °C	60s	1
	Storage	12 °C	∞	Storage

Table S4: PCR conditions used for genotyping FoxP1 and En1 genes.